

Crystal Structure Transformation in Chevrel Phase Mo_6S_8 Induced by Aluminum Intercalation

Linxiao Geng,^{†,‡} Jan P. Scheifers,^{‡,§} Jian Zhang,[§] Krassimir N. Bozhilov,^{§,||} Boniface P. T. Fokwa,^{*,‡,§} and Juchen Guo^{*,†,§}

[†]Department of Chemical and Environmental Engineering, University of California–Riverside, Riverside, California 92521, United States

[‡]Department of Chemistry, University of California–Riverside, Riverside, California 92521, United States

[§]Materials Science and Engineering Program, University of California–Riverside, Riverside, California 92521, United States

^{||}Central Facility for Advanced Microscopy and Microanalysis, University of California–Riverside, Riverside, California 92521, United States

Supporting Information

Electrochemical intercalation–extraction of aluminum (Al) in crystal host materials is an intriguing topic from both scientific and technological perspectives. Rechargeable Al-ion batteries based on intercalation chemistry may potentially be feasible for large-scale energy storage applications. However, Al^{3+} ions are inherently difficult to intercalate into crystal structures due to their strong Coulombic attraction to the anionic framework.^{1–3} Despite the surging interest in electrochemical Al interactions with transition metal oxides and sulfides,^{1–12} unambiguous reversible Al intercalation has only been observed in Chevrel phase molybdenum sulfide (Mo_6S_8).^{4,5} Figure 1a shows the Al intercalation–extraction cycling behavior in Mo_6S_8 using constant-current intercalation (discharge) and constant-current-constant-voltage (CCCV) extraction (charge) at 50 °C. As displayed in Figure 1b, a very stable and reversible capacity of approximately 105 mAh g^{−1} can be achieved despite the noticeable irreversibility in the first cycle.

Although promising capacity has been demonstrated, the Al intercalation process and the induced structural change of Mo_6S_8 are not well understood. On the other hand, the mechanism of magnesium (Mg) intercalation in Mo_6S_8 has been intensively investigated.^{13–16} It is well recognized that intercalation of Mg^{2+} ions into Mo_6S_8 induces two distinct phase transitions represented by two intercalation potential plateaus. Mg^{2+} ions first intercalate in the preferred sites within the rhombohedron made from eight Mo_6S_8 clusters (inner sites) to form the $\text{Mg}_1\text{Mo}_6\text{S}_8$ structure. In the second intercalation step, Mg^{2+} ions occupy the sites in each face of the rhombohedron (outer sites), a process facilitated by the repulsion from the Mg^{2+} ions in the inner sites, to form the $\text{Mg}_2\text{Mo}_6\text{S}_8$ structure.¹⁵ The electrochemical intercalation of Zn^{2+} cations into Mo_6S_8 has also been reported to have the similar intercalation mechanism as the Mg^{2+} cations.^{17,18} Lee et al. adopted the Mg intercalation mechanism to describe the process of Al intercalation in Mo_6S_8 .⁵ They propose that Al^{3+} ions exclusively occupy the inner sites during the first step (the first intercalation plateau at ~0.5 V shown in Figure 1a) to form the $\text{Al}_1\text{Mo}_6\text{S}_8$ structure, and that in the second step (the second intercalation plateau in Figure 1a), Al^{3+} ions occupy the outer site to form a new structure of $\text{Al}_{4/3}\text{Mo}_6\text{S}_8$. However,

given the much smaller cation size and stronger electrostatic repulsion of Al^{3+} , which can overcome the preference of the inner sites, we hypothesize that the intercalation process of Al^{3+} differs from that of Mg^{2+} as supported by our experimental findings below.

Chevrel phase $\text{Cu}_2\text{Mo}_6\text{S}_8$ was first synthesized via a solid-state reaction of the elements in stoichiometric ratio.¹⁹ Copper was thoroughly removed in hydrochloric acid with bubbling oxygen to obtain the pristine Mo_6S_8 (Figure S1 and Table S1 in Supporting Information). Figure 2a shows the high-resolution transmission electron microscopy (HRTEM) image of the synthesized Mo_6S_8 with selected area electron diffraction (SAED) pattern. As illustrated in the left panel of Figure 2b, the Mo_6S_8 cluster is composed of a Mo octahedron inside of a distorted eight-sulfur cube. The crystal structure of Mo_6S_8 belongs to $\bar{R}\bar{3}$ space group with $a = b = 9.1833(3)$ Å and $c = 10.8716(5)$ Å.²⁰ The right panel of Figure 2b displays the two types of sites accommodating intercalated Al in the Mo_6S_8 crystal: six sites inside the rhombohedron made from eight Mo_6S_8 clusters (inner sites Al_1 , orange) and two sites in each face of the rhombohedron (outer sites Al_2 , yellow).

The inset of Figure 2c displays the electrochemical potential profile of Al intercalation in Mo_6S_8 from the galvanostatic intermittent titration technique (GITT). The near-equilibrium potential profile of Al intercalation shows three stages: a short plateau between 0.95 and 0.85 V, a long plateau between 0.52 and 0.45 V, and a short plateau at 0.35 V vs Al^{3+}/Al . On the basis of the GITT profile, we prepared three Al intercalated samples ($\text{Al}_x\text{Mo}_6\text{S}_8$) at different intercalation stages using the galvanostatic method with a small current (2 mA g^{−1}) to ensure maximal intercalation. As shown in Figure 2c, Point A is the pristine Mo_6S_8 , and Points B ($E = 0.58$ V), C ($E = 0.4$ V) and D ($E = 0.3$ V) represent the end of each of the three potential plateaus identified by GITT. The *ex situ* powder XRD patterns (Figure 2d) obtained on these three $\text{Al}_x\text{Mo}_6\text{S}_8$ samples demonstrate distinct structural evolution of Mo_6S_8 .

Received: August 5, 2018

Revised: November 15, 2018

Published: November 16, 2018

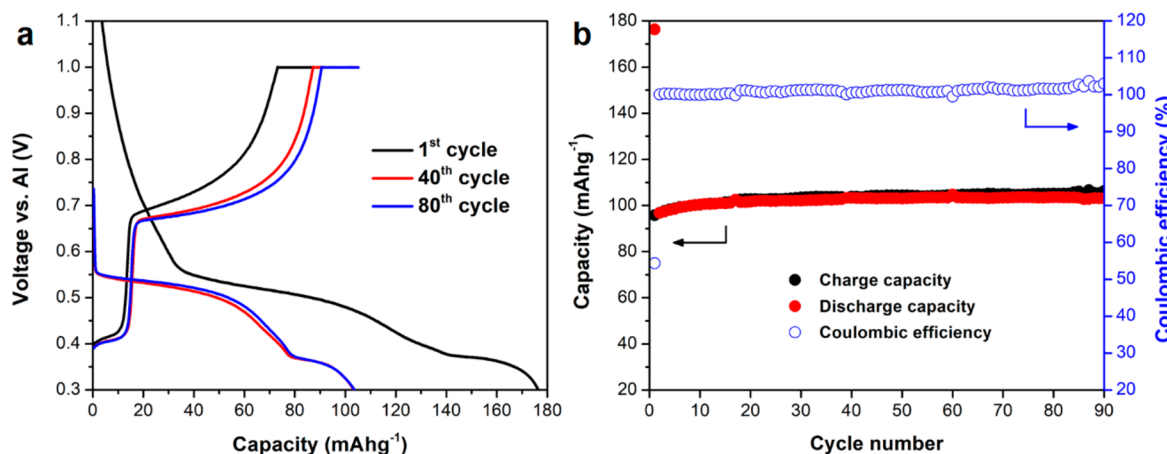


Figure 1. (a) The 1st, 40th, and 80th constant-current discharge and CCCV charge curves; (b) the cycle stability of Al vs Mo₆S₈ at 50 °C with 40 mA g⁻¹ current density.

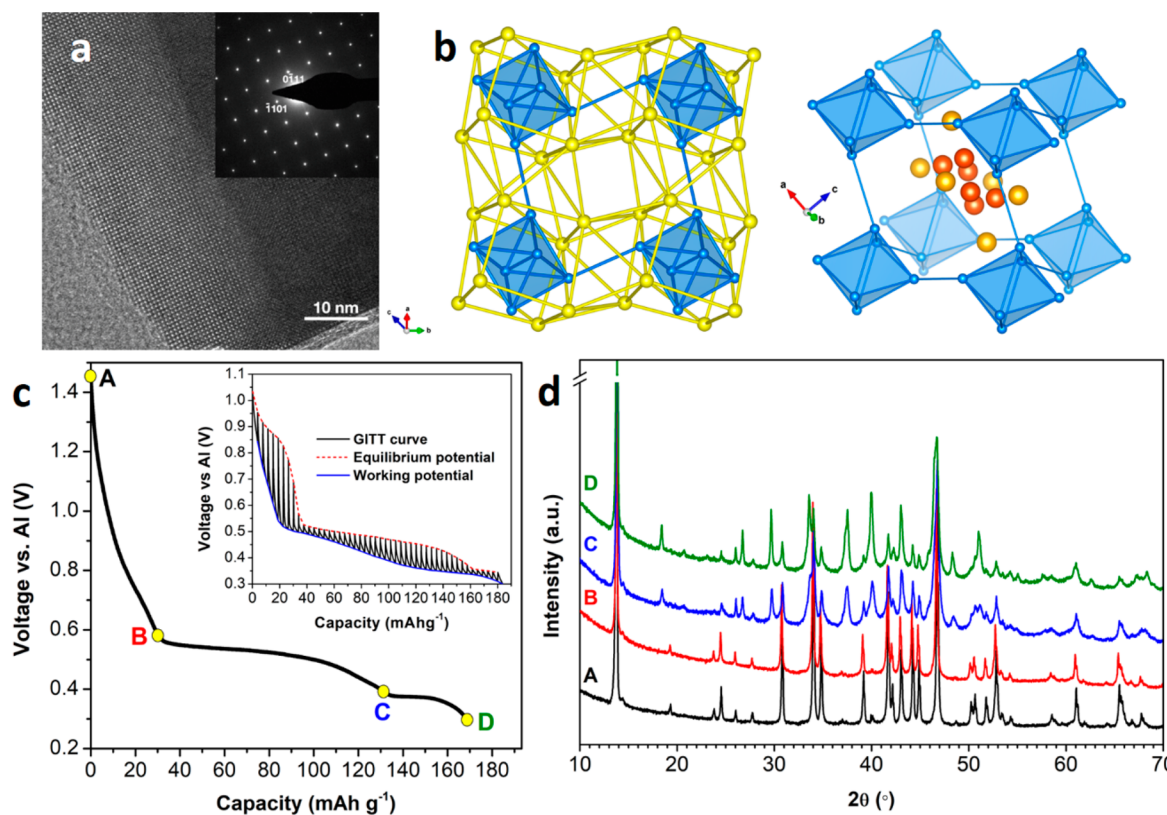


Figure 2. (a) HRTEM image of Mo₆S₈ and the corresponding electron diffraction pattern along zone axis [10-11] as inset, (indexed in hexagonal unit cell); (b) illustration of Mo₆S₈ crystal structure and the two types of Al sites (inner sites Al₁ in orange and outer sites Al₂ in yellow, sulfur atoms omitted for clarity); (c) potential profile of galvanostatic Al intercalation in Mo₆S₈ at 50 °C (GITT profile as the inset); (d) *ex situ* XRD patterns of Al intercalated Mo₆S₈ at different potentials indicated in panel c.

during the Al intercalation. Specifically, The XRD pattern at Point B is identical to that of the pristine Mo₆S₈ while Point C shows new peaks emerging at 18.7°, 27°, 30°, 34°, 37.7°, 40.2°, 48.5°, and 51.3° and peaks diminishing at 19.5°, 24°, 24.5°, 30.9°, 34°, 34.8°, 39°, 42°, 44.5°, 45°, 53°, and 65.5°. The intensities of the new peaks continue to increase at Point D. The content of Al in Al_xMo₆S₈ is determined by two methods: scanning electron microscopy with energy dispersive X-ray (EDX) spectroscopy (Figures S2 to S4 and Tables S2 to S4 in Supporting Information) and inductively coupled plasma optical emission spectroscopy (ICP-OES). Al is not detected

by either EDX or ICP-OES in the Al_xMo₆S₈ sample at Point B ($x = 0$). The chemical compositions according to EDX at Points C and D are Al_{1.06(1)}Mo₆S₈ and Al_{1.46(1)}Mo₆S₈, respectively. The compositions at Points C and D measured by ICP-OES are Al_{1.16}Mo₆S₈ and Al_{1.48}Mo₆S₈, respectively. The results from both EDX and ICP-OES agree closely with the intercalation capacity at these two points. It is also worth noting that chlorine was not detected in any Al_xMo₆S₈ samples, which clearly indicates Al³⁺ cation desolvation occurs at the Mo₆S₈ surface during intercalation. Wan and co-workers' investigation²¹ on the desolvation mechanism during Mg²⁺

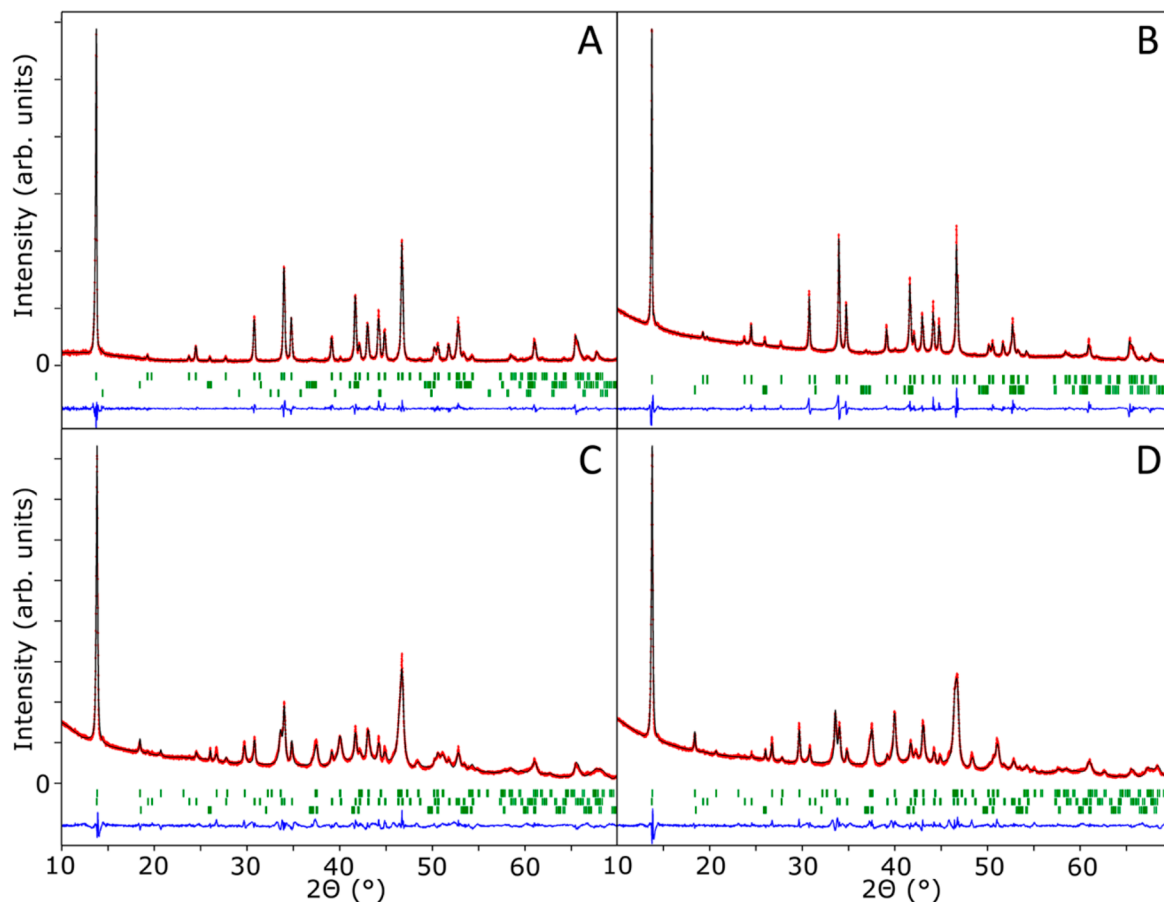


Figure 3. Rietveld refinements of the XRD data of the pristine Mo_6S_8 and $\text{Al}_x\text{Mo}_6\text{S}_8$ at different intercalation stages shown in Figure 2d. Red curve is the measured data, black curve is the fit, and blue curve is the difference plot. Tick marks (green) indicate reflections for Mo_6S_8 (top) and MoO_2 (bottom) for panels A and B, and reflections for $\text{Al}_3\text{Mo}_6\text{S}_8$ (top), Mo_6S_8 (middle) and MoO_2 (bottom) for panels C and D, respectively.

Table 1. Structural Properties of $\text{Al}_x\text{Mo}_6\text{S}_8$ from Rietveld Refinements

Point	Structure type(s)	a (Å)	c (Å)	Composition (wt %) ^c	x in $\text{Al}_x\text{Mo}_6\text{S}_8$	Occupancies Al_1/Al_2 (%)	R_{Bragg}
A	Mo_6S_8^a	9.190(1)	10.879(2)	99(1)	0	0/0	3.57
B	Mo_6S_8^a	9.194(1)	10.885(2)	98(1)	0	0/0	4.11
C	$\text{Al}_3\text{Mo}_6\text{S}_8^b$	9.6416(7)	10.001(1)	53(1)	1.49(1)	13/12	2.55
	Mo_6S_8^a	9.199(2)	10.878(3)	45(1)	0.6(1)	6/4	3.98
D	$\text{Al}_3\text{Mo}_6\text{S}_8^b$	9.640(2)	10.001(3)	68(2)	1.46(1)	13/11	3.02
	Mo_6S_8^a	9.202(4)	10.873(8)	31(1)	1.49(1)	16/9	3.81

^aInitial model ICSD-603588.²⁰ ^bInitial model ICSD-608604.²² ^c MoO_2 impurity was found in all samples and accounts for <2 wt %.

intercalation in Mo_6S_8 suggests the Mo cations on the surface can facilitate the desolvation of MgCl^+ and Mg_2Cl_3^+ by bonding to chloride anions, thus enabling Mg^{2+} intercalation. We speculate that similar desolvation may occur at the Mo_6S_8 surface during Al intercalation, which certainly is a critical process and warrants a separate investigation.

Rietveld refinements are performed on the four XRD patterns as shown in Figure 3 and summarized in Table 1. Both the XRD refinement result and TEM with SAED (Figure S5 in Supporting Information) confirm that the crystal structure at Point B is not changed from that of the pristine Mo_6S_8 . Similar observation was previously made by Lee et al., thus the first slope in the Al intercalation potential profile can be attributed to side-reactions of the electrolyte.⁵ More importantly, our refinement results clearly indicate the emerging of a new $\text{Al}_3\text{Mo}_6\text{S}_8$ -type structure at Points C and D, which is a distorted variant of Mo_6S_8 -type structure

belonging to the same space group $\bar{R}\bar{3}$ ($a = b = 9.640(2)$ – $9.6416(7)$ Å, $c = 10.001(1)$ – $10.001(3)$ Å).²²

From the unrestricted refinements in which all possible Al sites were refined freely (Table S5 in Supporting Information), we observe two different behaviors: the Al content in Al_1 and Al_2 sites is nearly equal in the $\text{Al}_3\text{Mo}_6\text{S}_8$ -type structure. On the contrary, Al occupancy has a site preference in the Mo_6S_8 -type structure as the Al_1 sites are always preferred over the Al_2 sites. However, the total amount of Al from the unrestricted refinement was unrealistic as it exceeded the maximum allowed in each type of site. In fact, the theoretical limit of Al occupancy in the Al_1 sites is 16.6% enforced by the electrostatic repulsion among the six symmetrically generated Al_1 cations being too close to each other, allowing for only 1 out of those six sites to be occupied. Therefore, we fixed the Al content using the EDX results as a basis while maintaining the occupancy preference found from the unrestricted refinement.

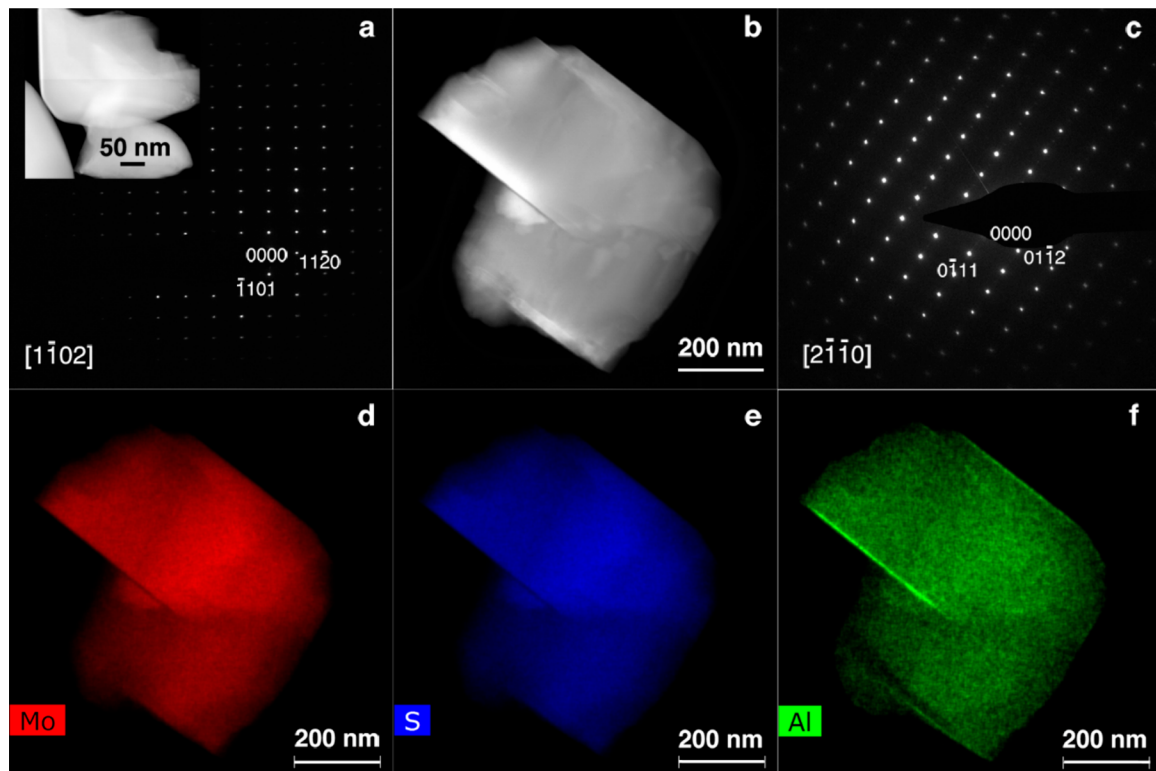


Figure 4. (a) SAED along zone axis $[1\bar{1}02]$ of $\text{Al}_{1.06(1)}\text{Mo}_6\text{S}_8$ at Point C with the corresponding HAADF STEM image as inset; (b) HAADF STEM image; (c) SAED along zone axis $[2\bar{1}\bar{1}0]$; (d–f) elemental mapping of $\text{Al}_{1.46(1)}\text{Mo}_6\text{S}_8$ at Point D.

The refinement results indicate an incomplete phase transition (53 wt %) from the Mo_6S_8 -type to the $\text{Al}_3\text{Mo}_6\text{S}_8$ -type structure during the first Al intercalation plateau (Point C) in Figure 2c. The occupancy of the Al_1/Al_2 sites in $\text{Al}_{1.06(1)}\text{Mo}_6\text{S}_8$ is 13%/12% in the $\text{Al}_3\text{Mo}_6\text{S}_8$ -type structure and 6%/4% in the Mo_6S_8 -type structure, indicating a slight Al_1 site preference in the pristine structure. During the second Al intercalation plateau (Point D), a further 15 wt % transformation from the Mo_6S_8 -type to the $\text{Al}_3\text{Mo}_6\text{S}_8$ -type structure is found in $\text{Al}_{1.46(1)}\text{Mo}_6\text{S}_8$. Interestingly, the occupancy of the Al_1/Al_2 sites in the $\text{Al}_3\text{Mo}_6\text{S}_8$ -type structure remains nearly constant (13%/11%), while a more pronounced sites preference is observed in the Mo_6S_8 -type structure: The Al_1 sites occupied by Al in the Mo_6S_8 -type structure increases to 16%, which is nearly twice the amount of the Al_2 sites occupied by Al (9%). The highest occupancy of 16% observed for the Al_1 site is close to the aforementioned theoretical limit of 16.6%, indicating that the maximum Al intercalation in Al_1 site has been reached. Rietveld refinements were also performed on XRD data at Points A to D with wider 2θ range from 10° to 140° . The wider-range refinements converged nicely for all samples and confirming the results in Figure 3 and Table 1 (Table S6 and Figure S6 in Supporting Information).

The obtained refinement results strongly indicate that the mechanism of Al intercalation in Mo_6S_8 is distinctly different from that of the Mg intercalation. Instead of Mg^{2+} cations consecutively occupying the inner sites and the outer sites inducing two distinct structural transformations, the intercalation of Al^{3+} cations results in only one new structure. Although the dynamics of the Al intercalation requires further investigation, we can hypothesize the Al intercalation process based on the crystallographic analysis: Al^{3+} cations initially intercalate into Mo_6S_8 with site preference to Al_1 over Al_2 ,

evidenced by the slight site preference observed in the Mo_6S_8 -type structure in $\text{Al}_{1.06(1)}\text{Mo}_6\text{S}_8$. However, the strong electrostatic repulsion between Al^{3+} cations rapidly repulses intercalating Al^{3+} to the Al_2 sites resulting in equal occupancy by Al in both sites in the newly formed $\text{Al}_3\text{Mo}_6\text{S}_8$ -type structure. The Mo_6S_8 -to- $\text{Al}_3\text{Mo}_6\text{S}_8$ structure transformation continues as Al^{3+} cations intercalating into Mo_6S_8 until a maximum 68 wt % phase transformation is reached. Interestingly, further Al^{3+} intercalation is mainly accommodated in the Mo_6S_8 -type structure with clear site preference to Al_1 and no structural transformation. This site preference is likely the reason for the occurrence of the second Al intercalation plateau between Point C and Point D.

The scanning transmission electron microscopy (STEM) imaging and analysis further provide evidence that $\text{Al}_{1.06(1)}\text{Mo}_6\text{S}_8$ at Point C and $\text{Al}_{1.46(1)}\text{Mo}_6\text{S}_8$ at Point D contain the same $\text{Al}_3\text{Mo}_6\text{S}_8$ -type structure. Figure 4a displays the SAED of $\text{Al}_{1.06(1)}\text{Mo}_6\text{S}_8$ along zone axis $[1\bar{1}02]$ with the high-angle annular dark-field (HAADF) STEM image as the inset. Reflections $\bar{1}101$ and $11\bar{2}0$ are labeled in Figure 4a and correspond to d -spacings of 6.4 and 4.8 Å, respectively. The distances are in good agreement with the lattice spacing from the $\text{Al}_3\text{Mo}_6\text{S}_8$ -type structure. Figure 4b,c shows the HAADF STEM image of a crystal of $\text{Al}_{1.46(1)}\text{Mo}_6\text{S}_8$ and its SAED pattern taken with electron beam along zone axis $[2\bar{1}\bar{1}0]$. Reflections $0\bar{1}11$ and $01\bar{1}2$ are labeled in Figure 4c, corresponding to d -spacings of 6.4 and 4.3 Å, respectively, which are also in good agreement with the lattice spacing expected of the $\text{Al}_3\text{Mo}_6\text{S}_8$ -type structure. Figure 4d–f displays the elemental mapping of the $\text{Al}_{1.46(1)}\text{Mo}_6\text{S}_8$ crystal shown in Figure 4b. Al is homogeneously distributed with a minor increase in concentration at crystal surfaces from electrolyte residue.

In summary, the Rietveld refinements of XRD on Al-intercalated Mo_6S_8 at different intercalation stages reveal a new $\text{Al}_3\text{Mo}_6\text{S}_8$ -type structure induced by the occupancy of Al in both the inner site and the outer site of Mo_6S_8 without preference due to the strong Al^{3+} – Al^{3+} repulsion. However, the Mo_6S_8 -to- $\text{Al}_3\text{Mo}_6\text{S}_8$ structural transformation is incomplete as further Al intercalation is accommodated by the original Mo_6S_8 -type structure with preference to the Al_1 site. This new mechanism could be due to the strong repulsion between Al^{3+} cations and their small size, which prohibits the exclusive occupation of the inner sites. This hypothesized mechanism is well supported by the results obtained from electrochemical analysis, microscopic studies, and X-ray diffraction. However, the crystal structure information at the static Al intercalation stages may not be sufficient to articulate the dynamics of the Al intercalation in Mo_6S_8 . It is also not clear why the Mo_6S_8 -to- $\text{Al}_3\text{Mo}_6\text{S}_8$ structural transformation remains incomplete. These two aspects are currently under investigation.

■ ASSOCIATED CONTENT

Supporting Information

The Supporting Information is available free of charge on the ACS Publications website at DOI: [10.1021/acs.chemmater.8b03312](https://doi.org/10.1021/acs.chemmater.8b03312).

Experimental details, EDX results of Chevrel phase Mo_6S_8 before and after Al intercalation at different stages, HAADF STEM image, electron diffraction and mapping of Al intercalated Mo_6S_8 at Point B, results of free refinements, and Rietveld refinements of wider-range XRD data from 10° to 140° ([PDF](#))

■ AUTHOR INFORMATION

Corresponding Authors

*B. P. T. Fokwa. E-mail: bfokwa@ucr.edu.
*J. Guo. E-mail: jguo@engr.ucr.edu.

ORCID

Jian Zhang: [0000-0003-0356-7611](https://orcid.org/0000-0003-0356-7611)
Boniface P. T. Fokwa: [0000-0001-9802-7815](https://orcid.org/0000-0001-9802-7815)
Juchen Guo: [0000-0001-9829-1202](https://orcid.org/0000-0001-9829-1202)

Author Contributions

[†]These authors contributed equally.

Notes

The authors declare no competing financial interest.

■ ACKNOWLEDGMENTS

L.G. and J.G. acknowledge the National Science Foundation for financial support under grant No. CAREER-1751929. The authors thank Prof. Gary Koenig in the Department of Chemical Engineering at University of Virginia for his help on the ICP-OES analysis.

■ REFERENCES

- (1) Rong, Z.; Malik, R.; Canepa, P.; Sai Gautam, G.; Liu, M.; Jain, A.; Persson, K.; Ceder, G. Materials design rules for multivalent ion mobility in intercalation structures. *Chem. Mater.* **2015**, *27*, 6016–6021.
- (2) Liu, M.; Jain, A.; Rong, Z.; Qu, X.; Canepa, P.; Malik, R.; Ceder, G.; Persson, K. A. Evaluation of sulfur spinel compounds for multivalent battery cathode applications. *Energy Environ. Sci.* **2016**, *9*, 3201–3209.
- (3) Geng, L.; Scheifers, J. P.; Fu, C.; Zhang, J.; Fokwa, B. P. T.; Guo, J. Titanium Sulfides as Intercalation-Type Cathode Materials for Rechargeable Aluminum Batteries. *ACS Appl. Mater. Interfaces* **2017**, *9*, 21251–21257.
- (4) Geng, L.; Lv, G.; Xing, X.; Guo, J. Reversible Electrochemical Intercalation of Aluminum in Mo_6S_8 . *Chem. Mater.* **2015**, *27*, 4926–4929.
- (5) Lee, B.; Lee, H. R.; Yim, T.; Kim, J. H.; Lee, J. G.; Chung, K. Y.; Cho, B. W.; Oh, S. H. Investigation on the Structural Evolutions during the Insertion of Aluminum Ions into Mo_6S_8 Chevrel Phase. *J. Electrochem. Soc.* **2016**, *163*, A1070–A1076.
- (6) Jayaprakash, N.; Das, S. K.; Archer, L. A. The Rechargeable Aluminum-Ion Battery. *Chem. Commun.* **2011**, *47*, 12610–12612.
- (7) Reed, L. D.; Menke, E. The Roles of V_2O_5 and Stainless Steel in Rechargeable Al-Ion Batteries. *J. Electrochem. Soc.* **2013**, *160*, A915–A917.
- (8) Chiku, M.; Takeda, H.; Matsumura, S.; Higuchi, E.; Inoue, H. Amorphous Vanadium Oxide/Carbon Composite Positive Electrode for Rechargeable Aluminum Battery. *ACS Appl. Mater. Interfaces* **2015**, *7*, 24385–24389.
- (9) Wang, H.; Bai, Y.; Chen, S.; Luo, X.; Wu, C.; Wu, F.; Lu, J.; Amine, K. Binder-Free V_2O_5 Cathode for Greener Rechargeable Aluminum Battery. *ACS Appl. Mater. Interfaces* **2015**, *7*, 80–84.
- (10) Gu, S.; Wang, H.; Wu, C.; Bai, Y.; Li, H.; Wu, F. Confirming Reversible Al^{3+} Storage Mechanism Through Intercalation of Al^{3+} into V_2O_5 Nanowires in a Rechargeable Aluminum Battery. *Energy Storage Mater.* **2017**, *6*, 9–17.
- (11) Wang, F.; Liu, Z.; Wang, X.; Yuan, X.; Wu, X.; Zhu, Y.; Fu, L.; Wu, Y. A conductive polymer coated MoO_3 anode enables an Al-ion capacitor with high performance. *J. Mater. Chem. A* **2016**, *4*, 5115–5123.
- (12) Gonzalez, J. R.; Nacimiento, F.; Cabello, M.; Alcantara, R.; Lavela, P.; Tirado, J. L. Reversible intercalation of aluminium into vanadium pentoxide xerogel for aqueous rechargeable batteries. *RSC Adv.* **2016**, *6*, 62157–62164.
- (13) Aurbach, D.; Lu, Z.; Schechter, A.; Gofer, Y.; Gizbar, H.; Turgeman, R.; Cohen, Y.; Moshkovich, M.; Levi, E. Prototype systems for rechargeable magnesium batteries. *Nature* **2000**, *407*, 724–727.
- (14) Levi, M. D.; Lancry, E.; Gizbar, H.; Gofer, Y.; Levi, E.; Aurbach, D. Phase transitions and diffusion kinetics during Mg^{2+} - and Li^+ -ion insertions into the Mo_6S_8 chevrel phase compound studied by PITT. *Electrochim. Acta* **2004**, *49*, 3201–3209.
- (15) Levi, E.; Lancry, E.; Mitelman, A.; Aurbach, D.; Ceder, G.; Morgan, D.; Isnard, O. Phase Diagram of Mg Insertion into Chevrel Phases, $\text{Mg}_x\text{Mo}_6\text{T}_8$ ($\text{T} = \text{S}, \text{Se}$). I. Crystal Structure of the Sulfides. *Chem. Mater.* **2006**, *18*, 5492.
- (16) Ling, C.; Suto, K. Thermodynamic Origin of Irreversible Magnesium Trapping in Chevrel Phase Mo_6S_8 : Importance of Magnesium and Vacancy Ordering. *Chem. Mater.* **2017**, *29*, 3731–3739.
- (17) Cheng, Y.; Luo, L.; Zhong, L.; Chen, J.; Li, B.; Wang, W.; Mao, S. X.; Wang, C.; Sprenkle, V. L.; Li, G.; Liu, J. Highly Reversible Zinc-Ion Intercalation into Chevrel Phase Mo_6S_8 Nanocubes and Applications for Advanced Zinc-Ion Batteries. *ACS Appl. Mater. Interfaces* **2016**, *8*, 13673–13677.
- (18) Chae, M. S.; Heo, J. W.; Lim, S. C.; Hong, S. T. Electrochemical Zinc-Ion Intercalation Properties and Crystal Structures of ZnMo_6S_8 and $\text{Zn}_2\text{Mo}_6\text{S}_8$ Chevrel Phases in Aqueous Electrolytes. *Inorg. Chem.* **2016**, *55*, 3294–3301.
- (19) Levi, E.; Gofer, Y.; Vestfreed, Y.; Lancry, E.; Aurbach, D. $\text{Cu}_2\text{Mo}_6\text{S}_8$ Chevrel Phase, A Promising Cathode Material for New Rechargeable Mg Batteries: A Mechanically Induced Chemical Reaction. *Chem. Mater.* **2002**, *14*, 2767–2773.
- (20) Tarascon, J. M.; Disalvo, F. J.; Murphy, D. W.; Hull, G. W.; Rietman, E. A.; Waszczak, J. V. Stoichiometry and physical properties of ternary molybdenum chalcogenides $\text{M}_x\text{Mo}_6\text{X}_8$ ($\text{X} = \text{S}, \text{Se}; \text{M} = \text{Li}, \text{Sn}, \text{Pb}$). *J. Solid State Chem.* **1984**, *54*, 204–212.
- (21) Wan, L. F.; Perdue, B. R.; Apblett, C. A.; Prendergast, D. Mg Desolvation and Intercalation Mechanism at the Mo_6S_8 Chevrel Phase Surface. *Chem. Mater.* **2015**, *27*, 5932–5940.

(22) Umarji, A. M.; Subba Rao, G. V.; Janawadkar, M. P.; Radhakrishnan, T. S. Metal atom incorporation studies on $A_xMo_6S_8$ Chevrel phases. *J. Phys. Chem. Solids* **1980**, *41*, 421–429.

Supporting Information

Crystal Structure Transformation in Chevrel Phase Mo₆S₈ Induced by Aluminum Intercalation

*Linxiao Geng,¹ Jan P. Scheifers,² Jian Zhang,³ Krassimir N. Bozhilov,^{3,4} Boniface P. T. Fokwa ^{*2,3} and Juchen Guo^{*1,3}*

1. Department of Chemical and Environmental Engineering, University of California, Riverside, California 92521, United States
2. Department of Chemistry, University of California, Riverside, California 92521, United States
3. Materials Science and Engineering Program, University of California, Riverside, California 92521, United States
4. Central Facility for Advanced Microscopy and Microanalysis, University of Riverside, California 92521, United States

Experimental Section

Synthesis of Chevrel Phase Mo₆S₈:

Chevrel phase Cu₂Mo₆S₈ was first synthesized via solid state reaction by heating stoichiometric mixture of elemental Cu, Mo and S powders. Stoichiometric amounts of Cu powder (Alfa Aesar, 10 micron, 99.9%), Mo powder (Alfa Aesar, 2-4 micron, 99.9%) and S powder (Sigma Aldrich 99.5-100.5%) were thoroughly mixed and then sealed in an evacuated quartz tube. The quartz tube was subsequently heated in a muffle furnace. The temperature ramp program was set to be as follows: The temperature was ramped up to 450 °C (1 °C min⁻¹) and hold for 24 h. The temperature was then ramped up to 700 °C (1 °C min⁻¹) and hold for another 24 h. The temperature was thereafter ramped up again to 1050 °C (1 °C min⁻¹) and hold for 48 h. Finally, the furnace was cooled down to room temperature naturally. The as synthesized Chevrel phase Cu₂Mo₆S₈ then underwent a chemical leaching process to yield the final product of Mo₆S₈ as follows: 300 mg Cu₂Mo₆S₈ was added into 20 ml 6M HCl solution. Oxygen was bubbled into the solution for 8

hours while stirring. After the reaction, the obtained Mo₆S₈ was centrifuged, washed with adequate amount of deionized water, and dried in vacuum oven at 50 °C overnight.

Electrode preparation:

The electrode slurry was made by mixing 80 wt.% Mo₆S₈, 10 wt.% carbon black, and 10 wt.% polystyrene (PS) in N-Methyl-2-pyrrolidone (NMP) solution via a mechanical mixer for 5 min in an argon-filled glovebox. For the cycling experiments, the slurry was then pasted on a carbon fiber paper current collector. It is noted that the carbon paper current collector is electrochemically inert in the voltage window of electrochemical tests proved by previous study. In the preparation of the Al intercalated Mo₆S₈ samples for XRD and TEM characterizations, the same slurry was coated on thin Mo foil (Alfa Aesar, 0.025mm, 99.95%) as the current collector. Therefore, the samples could be removed easily from the smooth Mo surface (than the porous carbon paper) after the galvanostatic Al intercalation.

Electrochemical analysis:

CR2016 coin cells were assembled in an argon-filled glovebox using Al foil (0.2 mm thickness, Alfa Aesar 99.9999%) as the anode. A single Whatman® glass fiber filter paper was used as the separator. The electrolyte was prepared by slowly adding anhydrous AlCl₃ (Sigma Aldrich 99.99%) into 1-butyl-3-methylimidazolium chloride (Sigma Aldrich 98%) with a molar ratio of 1.5:1 while stirring in the argon-filled glovebox. To prevent corrosion from the acidic electrolyte, tantalum foil (Sigma-Aldrich, 0.025mm thickness, 99.9%) was punched into discs of an appropriate size to be used as linings in the stainless-steel coin cell case. Cyclic voltammetry (CV) with a scan rate of 0.1 mV s⁻¹ and galvanostatic discharging and CCCV charging were performed with Gamry potentiostat Interface 1000 and Arbin battery test station, respectively, at both room temperature and 50°C. The GITT experiment was performed on Arbin battery test station at 50°C: Al was

intercalated into the Mo_6S_8 at a current density of 16 mA g^{-1} for 15 minutes followed by a resting step of 2 hours. The intercalation-rest process was repeated until the potential reached the cut-off limit at 0.3 V vs Al.

Materials characterization:

SEM was performed with a FEI XL30-FEG. TEM and STEM was performed at 300 kV accelerating voltage in a Thermo Scientific Titan Themis 300 instrument, fitted with X-FEG electron source, 3 lens condenser system, S-Twin objective lens, and SuperX energy-dispersive X-ray spectrometer (EDX). The EDX system incorporates 4 symmetrically arranged 30 mm^2 windowless SDD detectors with 0.7 srad collection angle. High-resolution TEM images were recorded at resolution of 2048×2048 pixels with a FEI CETA-16M CMOS digital camera with beam convergence semi-angle of about 0.08 mrad . STEM images were recorded with Fischione Instruments Inc. Model 3000 High Angle Annular Dark Field (HAADF) Detector with probe current of 150 pA , frame size of 2048×2048 , dwell time of $15 \text{ } \mu\text{sec/pixel}$, and camera length of 195 mm . The XRD characterization was conducted using a PANalytical EMPYREAN instrument ($45 \text{ kV}/40 \text{ mA}$) with a Cu- K_α source ($\lambda = 1.543 \text{ \AA}$) over the course of 2 hours to obtain high quality XRD data. The XRD data were analyzed by applying the Rietveld¹ refinement method as implemented in FullPROF.² The Al content in the $\text{Al}_x\text{Mo}_6\text{S}_8$ samples (Points B, C, and D) was determined by EDX and inductively coupled plasma optical emission spectroscopy (ICP-OES) analysis (PerkinElmer Optima 8000). Prior to the XRD, TEM, EDX, and ICP-OES analyses, the $\text{Al}_x\text{Mo}_6\text{S}_8$ samples were thoroughly washed to remove the electrolyte residue from the surface with following procedure: The cells after Al intercalation were disassembled in the glovebox to extract the $\text{Al}_x\text{Mo}_6\text{S}_8$ samples. The samples were first rinsed with anhydrous tetrahydrofuran (THF) multiple times to get rid of the superficial ionic liquid electrolyte residue. The rinsing was

performed in the glovebox. The $\text{Al}_x\text{Mo}_6\text{S}_8$ samples were then soaked in NMP solvent in centrifuge tubes to dissolve the PS binder, followed by centrifuge at 4000 rpm for 10 min to separate the $\text{Al}_x\text{Mo}_6\text{S}_8$ samples from the solvent. The samples were further washed three times using adequate amount of THF by bath-sonication and vortex shaking to completely remove all the electrolyte residue. The samples were finally dried in the vacuum oven at 50 °C before the characterizations. To prepare the $\text{Al}_x\text{Mo}_6\text{S}_8$ samples for ICP-OES analysis, appropriate amounts of samples were dissolved in aqua regia and then diluted to meet the concentration requirements of the instrument, typically in the range of 0.1 to 10 ppm.

Reference:

- (1) D. S. Young, B. S. Sachais, L. C. Jefferies, **1993**, The Rietveld method.
- (2) J. Rodriguez-Carvajal, *In satellite meeting on powder diffraction of the XV congress of the IUCr*, **1990**, 127, Toulouse, France.

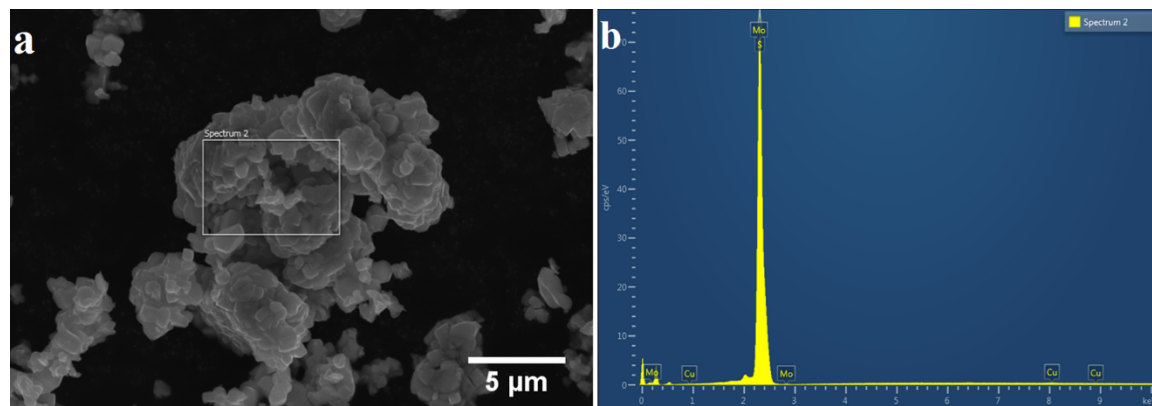


Figure S1. EDX spectrum of the pristine Mo_6S_8 after leaching out Cu.

Table S1. Chemical composition of the pristine Mo_6S_8 . From the EDX analysis, the pristine Mo_6S_8 contains negligible amount of Cu.

Element	wt.%	Atomic %
S	29.95	56.13
Cu	0.01	0.01
Mo	70.04	43.86
Total:	100.00	100.00

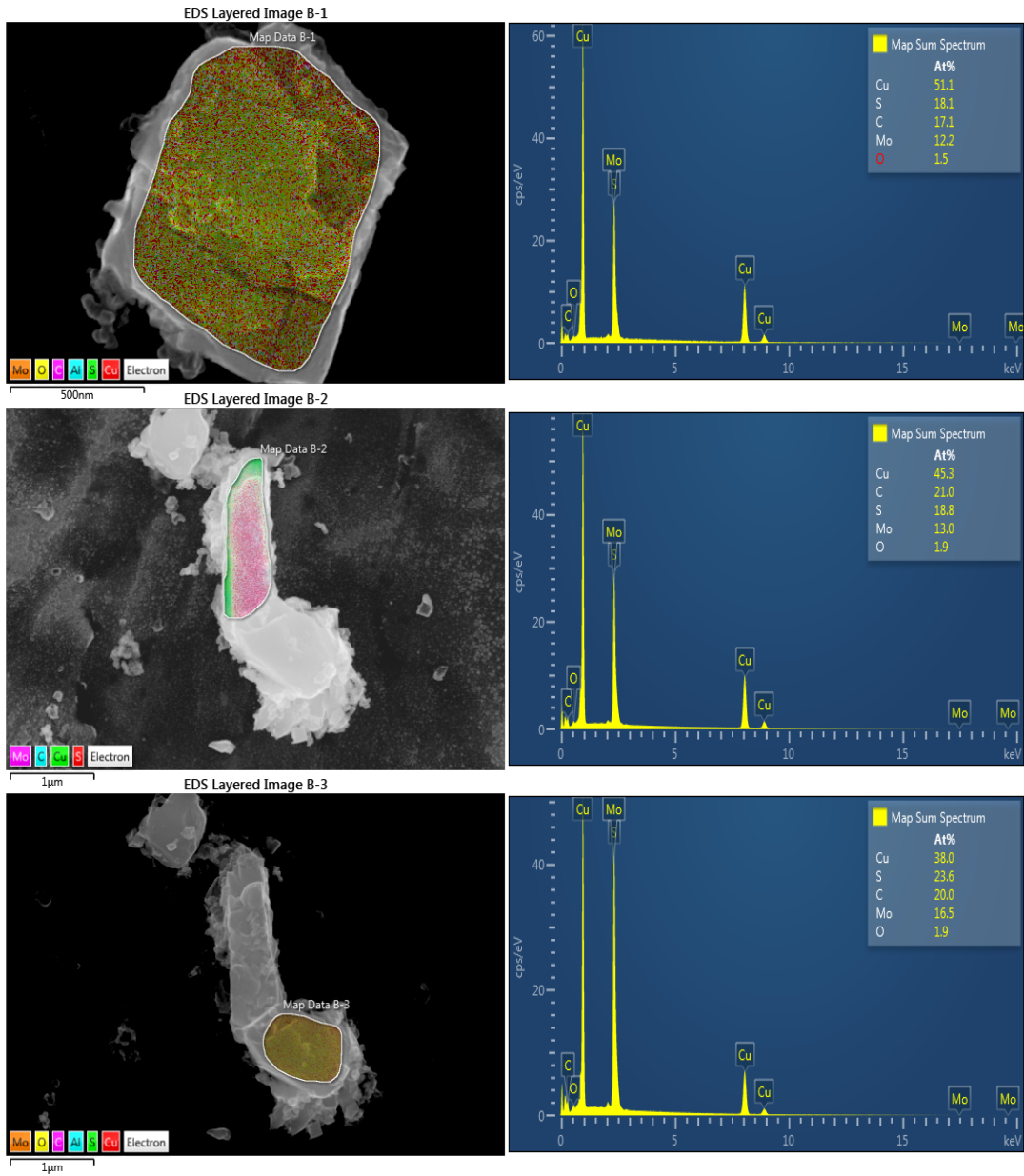


Figure S2. Three EDX spectra of the $\text{Al}_x\text{Mo}_6\text{S}_8$ sample obtained at Point B.

Table S2. Atomic ratio of elements in $\text{Al}_x\text{Mo}_6\text{S}_8$ at Point B, $x = 0$

	Map B-1	Map B-2	Map B-3
Cu (%)	51.1	45.3	38.0
S (%)	18.1	21.0	23.6
C (%)	17.1	18.8	20.0
Mo (%)	12.2	13.0	16.5
O (%)	1.5	1.9	1.9
x in $\text{Al}_x\text{Mo}_6\text{S}_8$	0	0	0

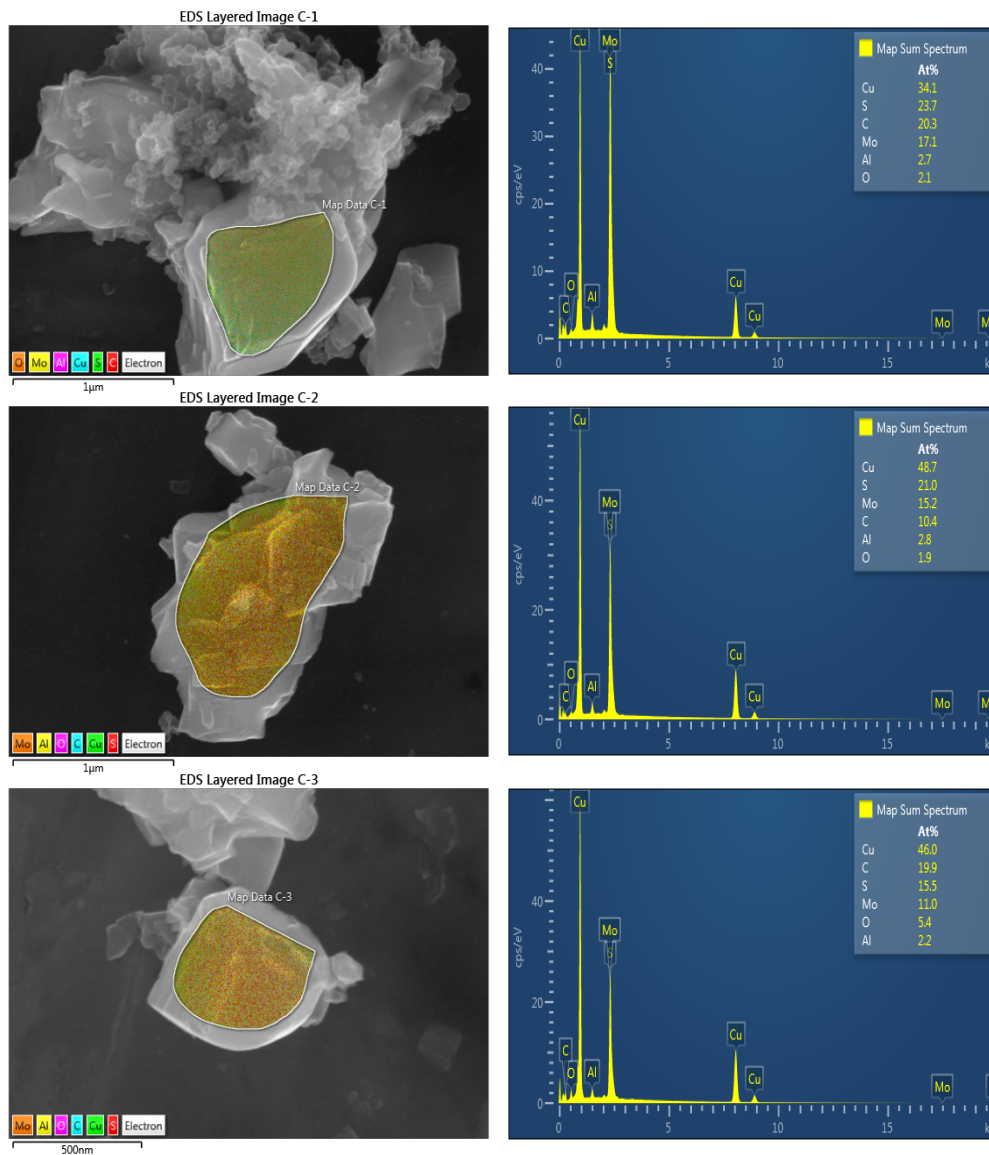


Figure S3. Three EDX spectra of the $\text{Al}_x\text{Mo}_6\text{S}_8$ sample obtained at Point C.

Table S3. Atomic ratio of elements in $\text{Al}_x\text{Mo}_6\text{S}_8$ at Point C, and $x = 1.057 \pm 0.120$

	Map C-1	Map C-2	Map C-3
Cu (%)	34.1	48.7	46.0
S (%)	23.7	21.0	15.5
C (%)	20.3	10.4	19.9
Mo (%)	17.1	15.2	11.0
O (%)	2.1	1.9	5.4
Al (%)	2.7	2.8	2.2
x in $\text{Al}_x\text{Mo}_6\text{S}_8$	0.926	1.083	1.162

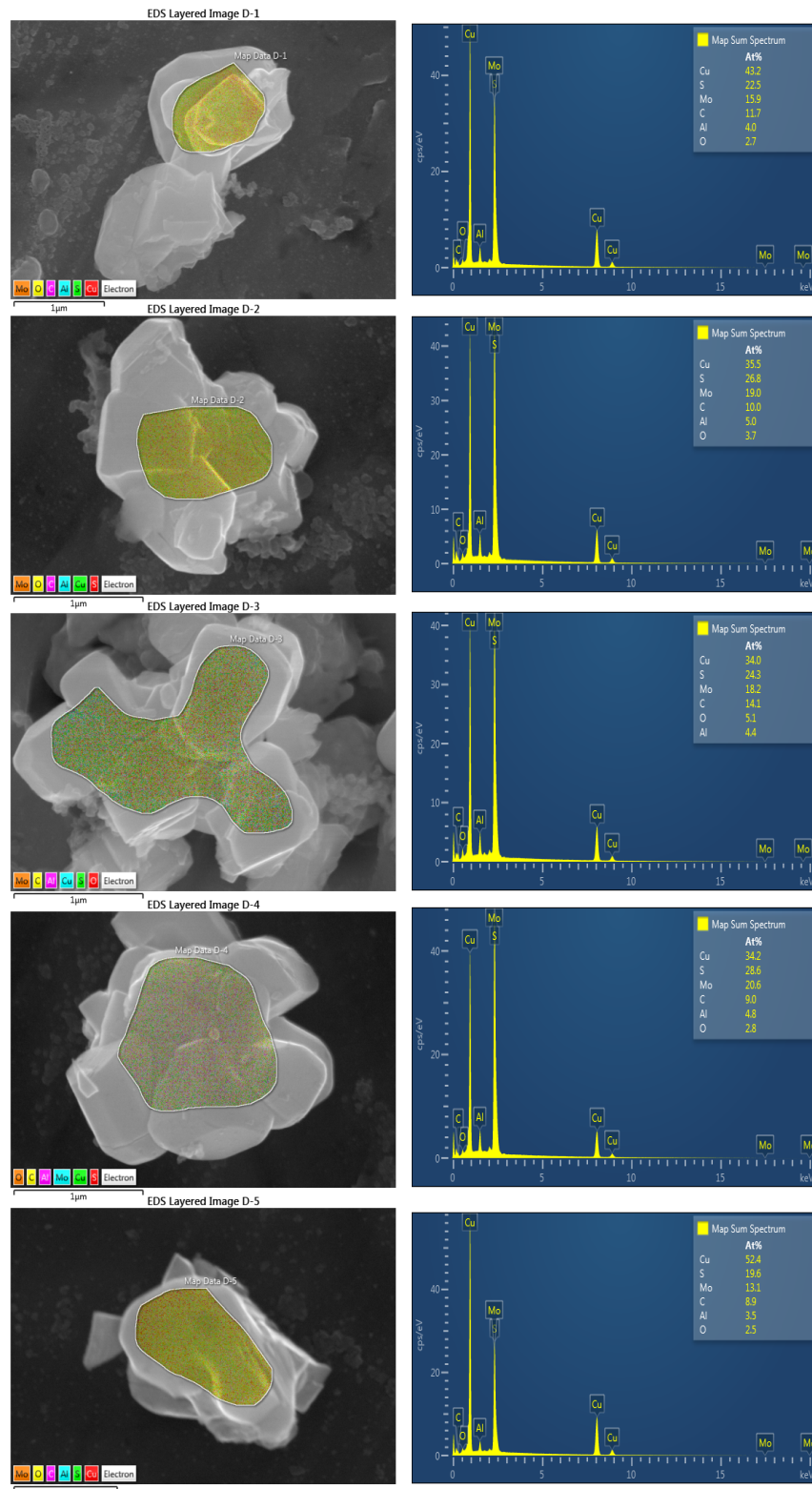


Figure S4. Five EDX spectra of the $\text{Al}_x\text{Mo}_6\text{S}_8$ sample obtained at Point D.

Table S4. Atomic ratio of elements in $\text{Al}_x\text{Mo}_6\text{S}_8$ at Point D, and $x = 1.460 \pm 0.061$.

	Map D-1	Map D-2	Map D-3	Map D-4	Map D-5
Cu (%)	43.2	35.5	34.0	34.2	52.4
S (%)	22.5	26.8	24.3	28.6	19.6
C (%)	11.7	10.0	14.1	9.0	8.9
Mo (%)	15.9	19.0	18.2	20.6	13.1
O (%)	2.7	3.7	5.1	2.8	2.5
Al (%)	4.0	5.0	4.4	4.8	3.5
x in $\text{Al}_x\text{Mo}_6\text{S}_8$	1.458	1.528	1.449	1.366	1.498

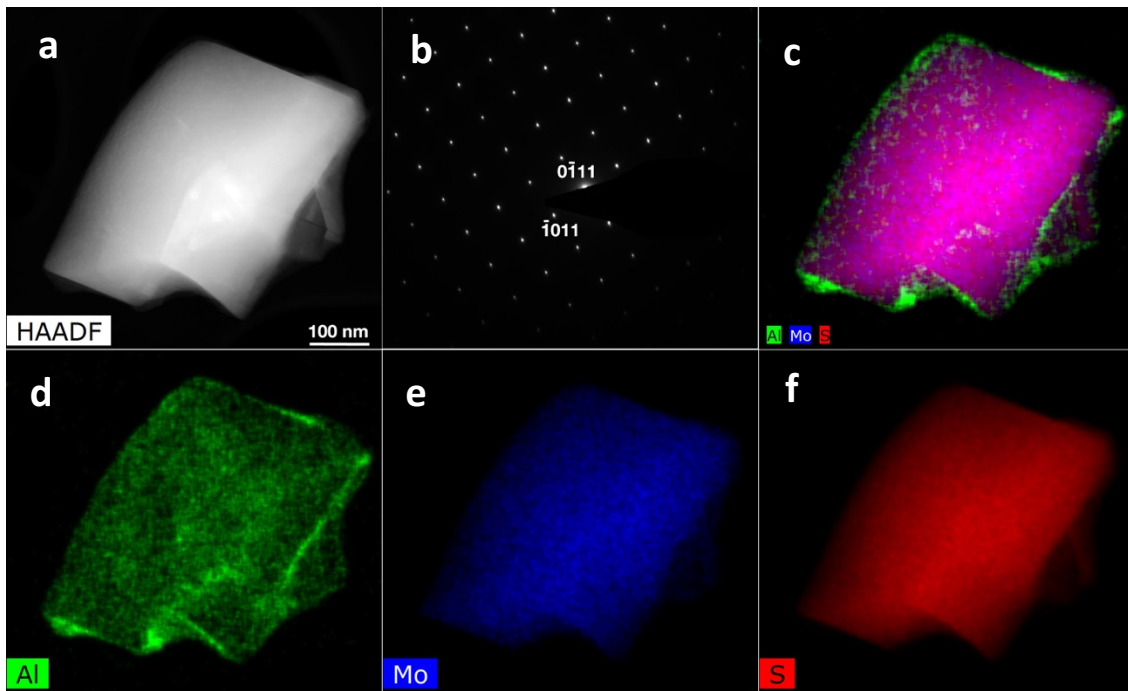


Figure S5. (a) The high-angle annular dark-field (HAADF) TEM image of Al intercalated Mo₆S₈ particle after the first intercalation slope (point B in Figure 3b); (b) The selected area diffraction pattern along zone axis [10 $\bar{1}$ 1] of Mo₆S₈ with reflections $[\bar{1}011]$ and $[0\bar{1}11]$ labeled (indexing in hexagonal unit cell); (c-f) elemental mapping of Al intercalated Mo₆S₈ at point B. The HAADF image shows a fractured Al intercalated Mo₆S₈ particle. The electron diffraction pattern clearly indicates the lattice parameters at this stage are still consistent with the original Mo₆S₈ structure. Therefore, no crystal phase transformation was induced in the first Al intercalation slope. The elemental mapping from the energy-dispersive X-ray spectroscopy (EDX) shows that majority of the Al does not enter the Mo₆S₈ structure and is only on the surface the particle resulted from the electrolyte residue.

Table S5. Results of the free refinements (no Al intercalation considered for points A and B).

Point	Phase	Wt.-%	Space group	a [Å]	c [Å]	Al1 occupancy (%)	Al2 occupancy (%)	x	R _{Bragg}
A	Mo ₆ S ₈	99(1)	R $\bar{3}$	9.190(1)	10.879(2)	0	0	0	3.57
	Al ₃ Mo ₆ S ₈	-	R $\bar{3}$	-	-	-	-	-	-
B	Mo ₆ S ₈	98(1)	R $\bar{3}$	9.194(1)	10.885 (2)	0	0	0	4.11
	Al ₃ Mo ₆ S ₈	-	R $\bar{3}$	-	-	-	-	-	-
C	Mo ₆ S ₈	40(1)	R $\bar{3}$	9.204(1)	10.882(2)	30(2)	18(1)	2.9(1)	2.14
	Al ₃ Mo ₆ S ₈	59(1)	R $\bar{3}$	9.625(2)	10.020(4)	59(2)	61(2)	7.2(2)	1.77
D	Mo ₆ S ₈	31(1)	R $\bar{3}$	9.202(2)	10.888(3)	78(5)	42(3)	7.2(4)	2.21
	Al ₃ Mo ₆ S ₈	69(2)	R $\bar{3}$	9.642(1)	10.009(2)	59(2)	47(2)	6.4(2)	2.56

Table S6. Atomic positions and further details on the free refinements. Axial divergence zero-angle offset (zero = -0.06) were corrected (asymmetric peak-shapes up to 30° 20 with asymmetry parameters Asym1 = 0.08 and Asym2 = 0.03) as obtained from a standard (SRM 640d) before the data collection. Atomic displacement parameters were not refined.

Site (Wyckoff)	Mo ₆ S ₈ (point A)	Al ₃ Mo ₆ S ₈ (point D)
Mo (18f)	0.8238(3) 0.8406(3) 0.3900(2)	0.1560(5) 0.1613(5) 0.3870(4)
S1 (6c)	0 0 0.221(8)	0 0 0.194(3)
S2 (18f)	0.969(7) 0.6841(7) 0.4205(6)	0.049(2) 0.339(2) 0.068(2)
Al1 (18f)	-	0.206(2) 0.126(3) -0.045(2)
Al2 (18f)	-	0.254(3) 0.182(4) 0.193(3)

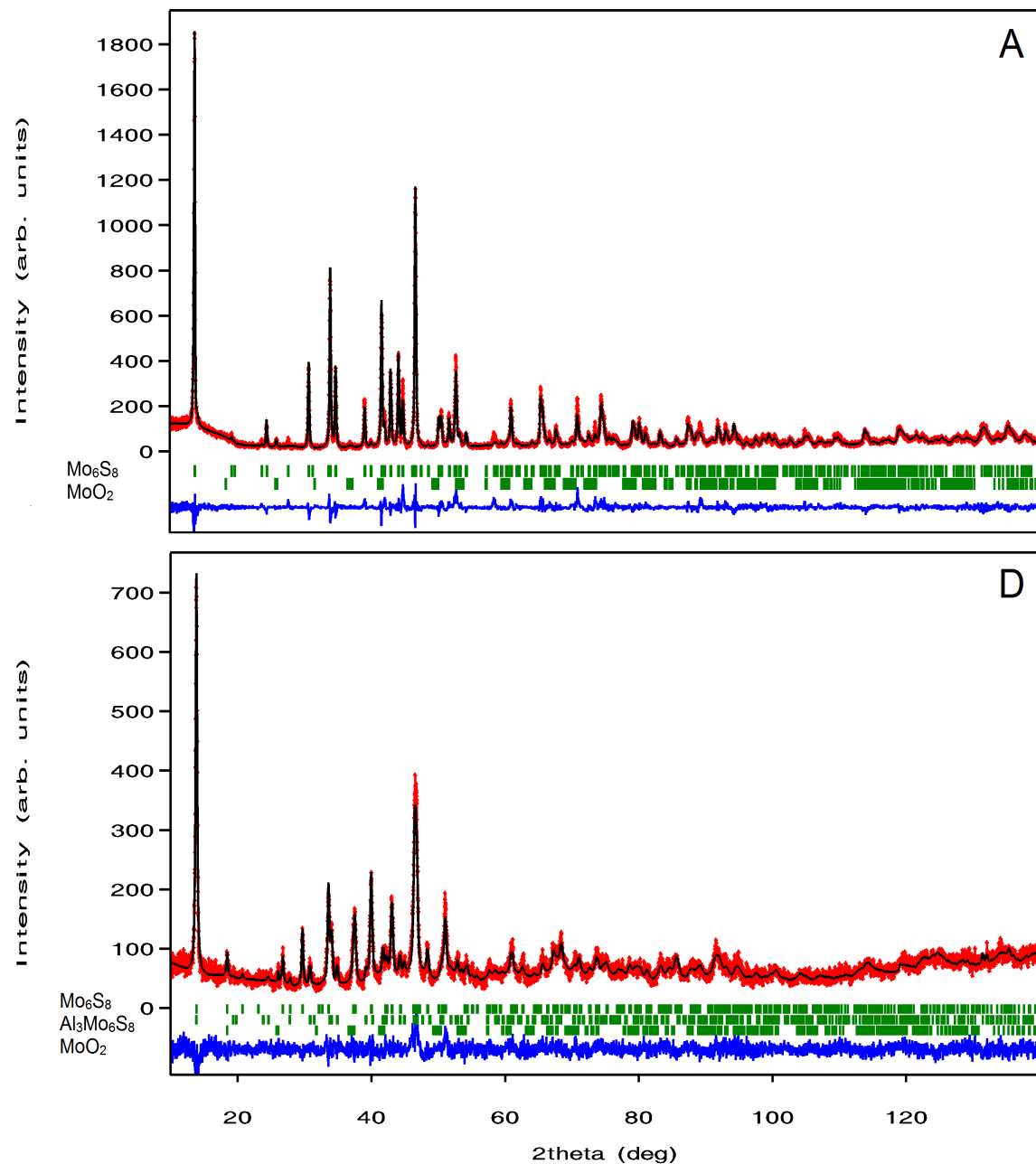


Figure S6. Rietveld refinements of full range ($10\text{-}140^\circ$ 2θ) X-ray powder diffraction measurements for points A and D.